university of groningen

University Medical Center Groningen

University of Groningen

# Reaction Layers around SiC Particles in Ti

Kooi, B.J.; Kabel, M.; Kloosterman, A.B.; Hosson, J.Th.M. De

*Published in:*
Acta Materialia

*DOI:*
10.1016/S1359-6454(99)00151-2

**IMPORTANT NOTE: You are advised to consult the publisher's version (publisher's PDF) if you wish to cite from it. Please check the document version below.**

*Document Version*
Publisher's PDF, also known as Version of record

*Publication date:*
1999

Link to publication in University of Groningen/UMCG research database

*Citation for published version (APA):*
Kooi, B. J., Kabel, M., Kloosterman, A. B., & Hosson, J. T. M. D. (1999). Reaction Layers around SiC Particles in Ti: An Electron Microscopy Study. *Acta Materialia*, *47*(10). https://doi.org/10.1016/S1359-6454(99)00151-2

**Copyright**
Other than for strictly personal use, it is not permitted to download or to forward/distribute the text or part of it without the consent of the author(s) and/or copyright holder(s), unless the work is under an open content license (like Creative Commons).

The publication may also be distributed here under the terms of Article 25fa of the Dutch Copyright Act, indicated by the “Taverne” license. More information can be found on the University of Groningen website: https://www.rug.nl/library/open-access/self-archiving-pure/taverne-amendment.

**Take-down policy**
If you believe that this document breaches copyright please contact us providing details, and we will remove access to the work immediately and investigate your claim.

*Downloaded from the University of Groningen/UMCG research database (Pure): http://www.rug.nl/research/portal. For technical reasons the number of authors shown on this cover page is limited to 10 maximum.*

Download date: 05-05-2023

PERGAMON

*Acta mater.* Vol. 47, No. 10, pp. 3105–3116, 1999
© 1999 Acta Metallurgica Inc.
Published by Elsevier Science Ltd. All rights reserved
Printed in Great Britain
PII: S1359-6454(99)00151-2
1359-6454/99 $20.00 + 0.00

# REACTION LAYERS AROUND SiC PARTICLES IN Ti: AN ELECTRON MICROSCOPY STUDY

**B. J. KOOI, M. KABEL, A. B. KLOOSTERMAN and J. TH. M. DE HOSSON†**

Department of Applied Physics, Materials Science Centre and Netherlands Institute for Metals Research, University of Groningen, Nijenborgh 4, 9747 AG Groningen, The Netherlands

*(Received 14 January 1999; accepted 25 March 1999)*

**Abstract**—A detailed description is given of the microstructure of the top layer of Ti–6Al–4V with SiC particles embedded with a high-power Nd:Yag laser system. Scanning electron microscopy (SEM), as well as conventional, analytical and high-resolution transmission electron microscopy (TEM) were used. An existing controversy about the presence or absence of $Ti_3SiC_2$ in the reactive SiC/Ti systems is clarified and the first observations of $Ti_5Si_3$ precipitation on stacking faults in Si supersaturated TiC are reported. The Si released during the reaction $SiC + Ti \rightarrow TiC + Si$ results in the formation of $Ti_5Si_3$. If in the reaction layer regions in between the TiC grains become enclosed, the rejected Si content increases locally and $Ti_3SiC_2$ plates with dominant (0001) facets nucleate. In the TiC grains particularly of the cellular reaction layer, a high density of widely extending stacking faults of the order of 100 nm is observed and on these faults in many instances small $Ti_5Si_3$ precipitates are present. © *1999 Acta Metallurgica Inc. Published by Elsevier Science Ltd. All rights reserved.*

*Keywords:* Laser treatment; Transmission electron microscopy (TEM); Titanium; Carbides; Microstructure

## 1. INTRODUCTION

Titanium exhibits several excellent properties, e.g. high strength-to-weight ratio and excellent corrosion resistance [1]. However, the tribological properties of Ti are relatively poor. In order to improve the wear resistance of Ti, SiC particles were embedded in a top layer (about 600 $\mu$m thick) of Ti–6Al–4V employing a high-power laser. The wear rate (weight loss) for abrasive wear diminished by a factor of seven for the SiC embedded Ti–6Al–4V compared to the untreated material (as tested under identical conditions). Also a pin on ring test for sliding wear under conditions of boundary lubrication indicated a substantial improvement because of the SiC particles embedded [2, 3]. Apparently the SiC particles are bonded well to the Ti matrix contributing to the improved wear resistance. The purpose of the present work is to provide a detailed description of the microstructure of the top layer of Ti–6Al–4V with embedded SiC particles derived on the basis of scanning electron microscopy (SEM), as well as using conventional, analytical and high-resolution transmission electron microscopy (TEM). Because of the high affinity of Ti for C an exothermic reaction $SiC + Ti \longrightarrow TiC + Si$ occurs during laser processing. Particularly, the influence of Si that is released during this reaction on the microstructure formed is scrutinized.

Reactions at interfaces between SiC and Ti have been studied extensively and only a few examples are given in Refs [4–12]. These studies were conducted on a wide variety of systems, ranging from, e.g. diffusion couples, fibre-reinforced metal matrix composites to laser-clad layers. Clearly similar, but also rather different results can be obtained for these systems which are mainly due to either similarities or differences in the actual heat treatments. For laser embedding SiC particles in Ti, the particles can be preplaced on the Ti surface [9, 10] or they can be injected into the laser melt pool [11, 12], which gives large differences in the respective heat absorption of the particles and the matrix and consequently result in very different microstructures. A particle injection process is used in the present work [2, 3] and the work is therefore most similar to the one reported in Refs [11, 12]. However, the present characterization of the microstructure is intended to be more comprehensive. An existing controversy about the presence or absence of $Ti_3SiC_2$ in the reactive SiC/Ti systems as explained in Ref. [8] will be clarified by the present work. Further, to the best of our knowledge this is the first report of observations of $Ti_5Si_3$ precipitation on stacking faults in Si supersaturated TiC.

## 2. EXPERIMENTAL

Single crystal 6H-SiC particles with a typical diameter of 80 $\mu$m were embedded in Ti–6Al–4V by employing a 2 kW continuous wave Rofin Sinar

†To whom all correspondence should be addressed.

Nd:YAG laser. Details about the laser process with controlled injection of particles in the melt pool are given in Refs [2, 3]. The laser beam is transported by means of fibre optics, resulting in a homogeneous intensity distribution. The diameter of the fibre is 0.8 mm, determining the minimum spot size. After leaving the fibre the beam is collimated before being focused to a spot diameter of about 3 mm. The lens system is water cooled and has a focal length of 120 mm. The spot size is obtained by setting the focal point of the laser 10 mm out of focus. Between the lens and the specimen a nozzle is located to supply a shielding gas protecting the lens and preventing oxidation of the specimen. The movement of the specimen is controlled by a CNC $X$–$Y$ table. The output power of the laser was varied from 1 up to 1.5 kW and the scan velocity ranged from 6 to 12 mm/s. A constant supply of powder to the substrate under the laser beam was provided by a powder feeding apparatus (Metco 9MP). The carrier gas for powder feeding can distort the melt bath. Therefore, a cyclone is used in which the major gas flow escapes through an upper outlet. Centrifugal forces prevent the powder from escaping from this outlet. The powder is fed through a bottom outlet with an amount of gas depending on the ratio of the diameters of the two outlets.

Specimens for TEM were prepared by grinding, dimpling and ion milling round 3 mm discs to electron transparency. The surface of the starting discs corresponded to the surface after laser embedding. By adjusting the amount of material removed from the top or the bottom of the discs, the TEM specimen corresponding to a certain chosen depth in the melt pool could be prepared. Ion milling was performed using two beams of 4 kV $Ar^+$ ions having an incidence angle of either 13° or 6° with the bottom and top side surfaces of the discs (using a Gatan dual ion mill 600 or a Gatan PIPS 691). Since the SiC was preferentially thinned by the $Ar^+$ ions, holes in the sample started in SiC regions. In this way electron-transparent regions in and around the SiC particles could be obtained rather nicely.

For TEM a JEOL 4000EX/II operating at 400 kV with a point-to-point resolution of 0.17 nm equipped with an on-axis Gatan 666 Parallel Electron Energy Loss Spectrometer located in Groningen was used. HRTEM images were obtained by digitizing negatives using a CCD camera and the gray scale was adapted to achieve reasonable brightness/contrast. HRTEM images were not filtered. For analytical TEM a JEOL 200 CX operating at 200 kV equipped with a Gatan 666 PEELS spectrometer as well as two Kevex system 8000 Energy Dispersive X-ray Spectroscopy (EDS) detectors located at the National Center for Electron Microscopy of the Lawrence Berkeley Laboratory was used. The EDS detectors comprise a high-angle detector with a resolution of 155 eV for Mn-$K_\alpha$ radiation and an ultra-thin window detector with a resolution of 109 eV for F-$K_\alpha$ radiation allowing quantitative analysis for elements with $Z \geq 6$. Although the used quantification procedures (performed with software at the NCEM) are standard-less for both PEELS and EDS, the procedures for quantification were calibrated internally on the embedded SiC particles. This allowed a relatively accurate quantification of the chemical composition of, e.g. TiC. For instance the ratios obtained of Si/C and of Ti/C are sensitive to the foil thickness during EDS analysis. By varying the foil thickness such that correct results are obtained for SiC and by measuring EDS spectra with well-comparable count rates for both SiC and TiC the composition of TiC could be obtained. Finally, the results of PEELS and EDX could be directly compared in a number of cases to check for consistency.

## 3. RESULTS AND DISCUSSION

### *3.1. TiC reaction layers and Si rejection in the melt pool*

SEM images of parts of the Ti–6Al–4V melt pool in which SiC particles were embedded are displayed in Fig. 1. Figure 1(a) corresponds to a location somewhat below the middle of the melt pool and Fig. 1(b) to the top region of the melt pool. Some different phases present have been indicated in the figures where the large black parts correspond to SiC. Around the SiC particles a reaction layer can be observed which is mainly composed of TiC (according to EDS in SEM and TEM, PEELS in TEM and to selected-area electron diffraction patterns of more than 100 grains). A PEELS spectrum identifying a TiC grain in the reaction layer is shown in Fig. 2. The higher affinity of Ti for C than Si gives rise to an exothermic reaction between Ti and SiC resulting in this TiC layer. The Si that is released during this exothermic reaction is rejected into the melt pool.

Near the bottom of the melt pool the dissolution of SiC is modest and the amount of Si rejected into the melt gives rise to a small amount of eutectic $Ti_5Si_3$/α-Ti on the grain boundaries of the α-Ti grains. In Fig. 1(a) the amount of eutectic has already increased due to the somewhat higher level in the melt pool causing an increased Si dissolution. Approaching the top of the melt pool the amount of Si rejected increases considerably and finally gives rise to large faceted pre-eutectic $Ti_5Si_3$ grains with eutectic $Ti_5Si_3$/α-Ti in between [see Fig. 1(b)]. Carbon can be in solid solution in $Ti_5Si_3$ up to about 8 at.%. Also TiC dendrites can be observed within the matrix region in between the SiC particles from about the middle to the top of the melt pool. The C/Ti ratio in the TiC dendrites is expected to be lower than in the TiC reaction layer

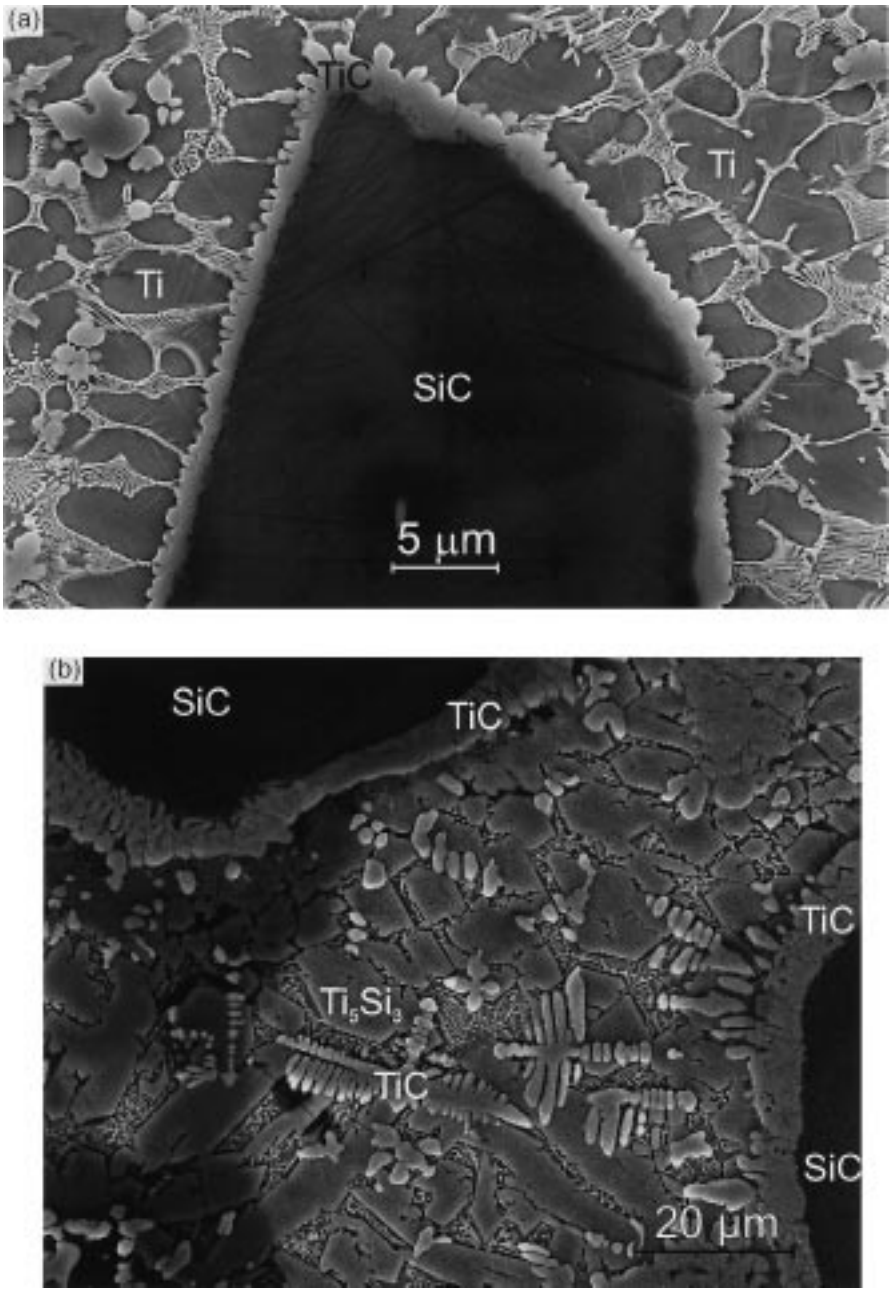


Fig. 1. SEM image of SiC particles laser embedded in Ti. Around the SiC particles a TiC reaction layer is formed due to an exothermic reaction between the SiC and Ti. (a) Region somewhat below the middle of the melt pool where the released Si results in eutectic $Ti_5Si_3$/Ti on the grain boundaries of Ti. The reaction layer is of the cellular type. (b) Region at the top of the melt pool where the released Si results in large faceted pre-eutectic $Ti_5Si_3$ grains surrounded by eutectic $Ti_5Si_3$/Ti. The reaction layer is of the cloud-like type.

giving a lower solidification temperature for the dendrites.

Actually two types of TiC reaction layers around the SiC particles were observed using SEM: (a) a cellular layer in which the TiC grains give the appearance of having been nucleated heterogeneously at the solid SiC/melt interface with subsequent cellular growth of the TiC into the melt [Fig. 1(a)]; (b) a cloud-like layer of spherical TiC grains pointing at "homogeneous" nucleation of the TiC within the melt very near to the solid SiC surface [more or less the case for the reaction layer observable in Fig. 1(b)].

### *3.2. $Ti_3SiC_2$ plates in the reaction layer*

TEM analysis of the cloud-like reaction layer revealed that besides a predominant fraction of spherical TiC grains also $Ti_3SiC_2$ plates appeared to

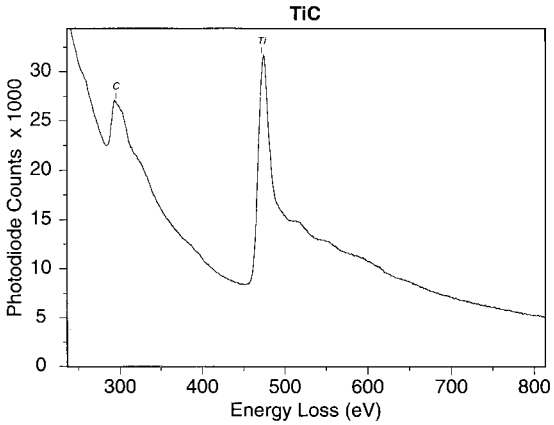


Fig. 2. A parallel electron energy loss spectrum identifying a TiC grain present in the reaction layer formed around the SiC particles embedded in the Ti–6Al–4V matrix. The reaction layer appears to be predominantly composed of TiC.

be present. Figure 3(a) shows a TEM overview of a cloud-like reaction layer in which the two phases TiC and $Ti_3SiC_2$ have been indicated for several grains. Much smaller $Ti_3SiC_2$ plates, not distinguishable in Fig. 3(a), are also present in the layer. The SiC particle, to which this layer was attached, has been removed by ion milling and was thus originally located in the region of the hole in the foil in Fig. 3(a). The $Ti_3SiC_2$ plates have dominant (0001) facets because they grow most easily along directions present within the basal plane. The identification of $Ti_3SiC_2$ is based on SAED patterns. Because of similarities in crystallography of 6H-SiC (with lattice parameters: $a = 0.308$ nm and $c = 1.509$ nm [13]) and of $Ti_3SiC_2$ (with $a = 0.306$ nm and $c = 1.764$ nm [14–17]) the diffraction patterns of the latter are at first sight easily misinterpreted being SiC. This is despite the fact that the $c$-lattice constants of the SiC poly-types are sufficiently different. A HRTEM image of $Ti_3SiC_2$ showing its 8H-like stacking is displayed in Fig. 3(b) with in the inset the simulated image for a thickness of 5 nm, a defocus values of −6 nm and a beam tilt of 1.3 mrad.

In the $Ti_3SiC_2$ stacking faults on basal planes and dislocations with Burgers vector $1/3\langle 11\bar{2}0\rangle$ were observed. The dislocations showed a tendency to be confined within a basal plane. In Fig. 4 a two-beam bright-field image (with other strong beam $g11\bar{2}0$) shows a $Ti_3SiC_2$ grain with a relatively large number of dislocations. In order to obtain strongly contrasting dislocations, the basal plane in Fig. 4 is tilted (with a tilt of about 12° out of the $\langle 01\bar{1}0\rangle$ zone axis). Examples of dislocations confined within the basal plane are indicated by an A; their dislocation lines have predominantly a horizontal component in the image. The B dislocations predominantly with a vertical line component in the image are not confined in the basal plane. Only recently the type of Burgers vector for dislocations in $Ti_3SiC_2$ was determined [18]. The $1/3\langle 11\bar{2}0\rangle$ Burgers vector is common for hexagonal crystals (corresponding to stacking of hexagonal planes) and in combination with the $(0001)\langle 11\bar{2}0\rangle$ slip system not striking. On the other hand the preference of the dislocation lines for confinement within a basal plane of $Ti_3SiC_2$ appears more interesting. This confinement is commonly observed and seems independent from the way the $Ti_3SiC_2$ is produced [18, 19]. The actual reason of interest is that the 8H-like stacking of $Ti_3SiC_2$ corresponds to the following repeat sequence of hexagonal planes: Ti–C–Ti–Si–Ti–C where the C atoms can be regarded as located in interstitial sites. Hence, the Si or C planes are in between two Ti planes and no adjacent Si and C planes occur. Now the confinement of the dislocations within a basal plane of $Ti_3SiC_2$ may indicate that the dislocation core has a preference for a certain basal-plane type. For instance the core may have a preference to be directly linked to an Si basal plane, because in between the Si and Ti planes the interstitial sites are free from C. In the same context, also certain types of stacking faults in $Ti_3SiC_2$ will be preferential over others. To provide more precise answers to these questions of the location of dislocation cores and stacking faults, HRTEM observations are required, which will be published elsewhere.

TEM analysis of the cellular reaction layer did not reveal the presence of $Ti_3SiC_2$. The different way in which the Si is rejected from the TiC grains in the two types of reaction layers can be held responsible for the presence or absence of $Ti_3SiC_2$. In the case of the cloud-like reaction layer volumes in between the TiC grains can become enclosed, preventing the rejection of an excess Si into the melt pool. In the enclosed volumes the Si concentration is subsequently raised sufficiently to nucleate at the interface between TiC and SiC the phase $Ti_3SiC_2$, in accordance with the ternary Ti–Si–C phase diagram (which is only known for the temperature range 1100–1250°C [15, 20, 21]). This sequence of a primary TiC nucleation followed by a nucleation of $Ti_3SiC_2$ can be expected because the melting point of TiC is probably highest, that is to say: 3061°C for TiC, 2545°C for SiC and a melting point for $Ti_3SiC_2$ probably in between. In the case of the cellular reaction layer Si areas in the material do not become trapped and accordingly $Ti_3SiC_2$ is not observed. The excess of Si rejected into the "open" melt results in accordance with the ternary Ti–Si–C phase diagram in the nucleation of $Ti_5Si_3$ at the interface between TiC and Ti. This occurs around both types of reaction layers. The Al and V present in the original Ti–6Al–4V is according to EDS in TEM present in $Ti_5Si_3$ and α-Ti and not detectably present in TiC.

The present sequence of primary TiC formation followed by $Ti_3SiC_2$ at the "interface" between TiC and SiC if sufficient supersaturation with Si occurs,

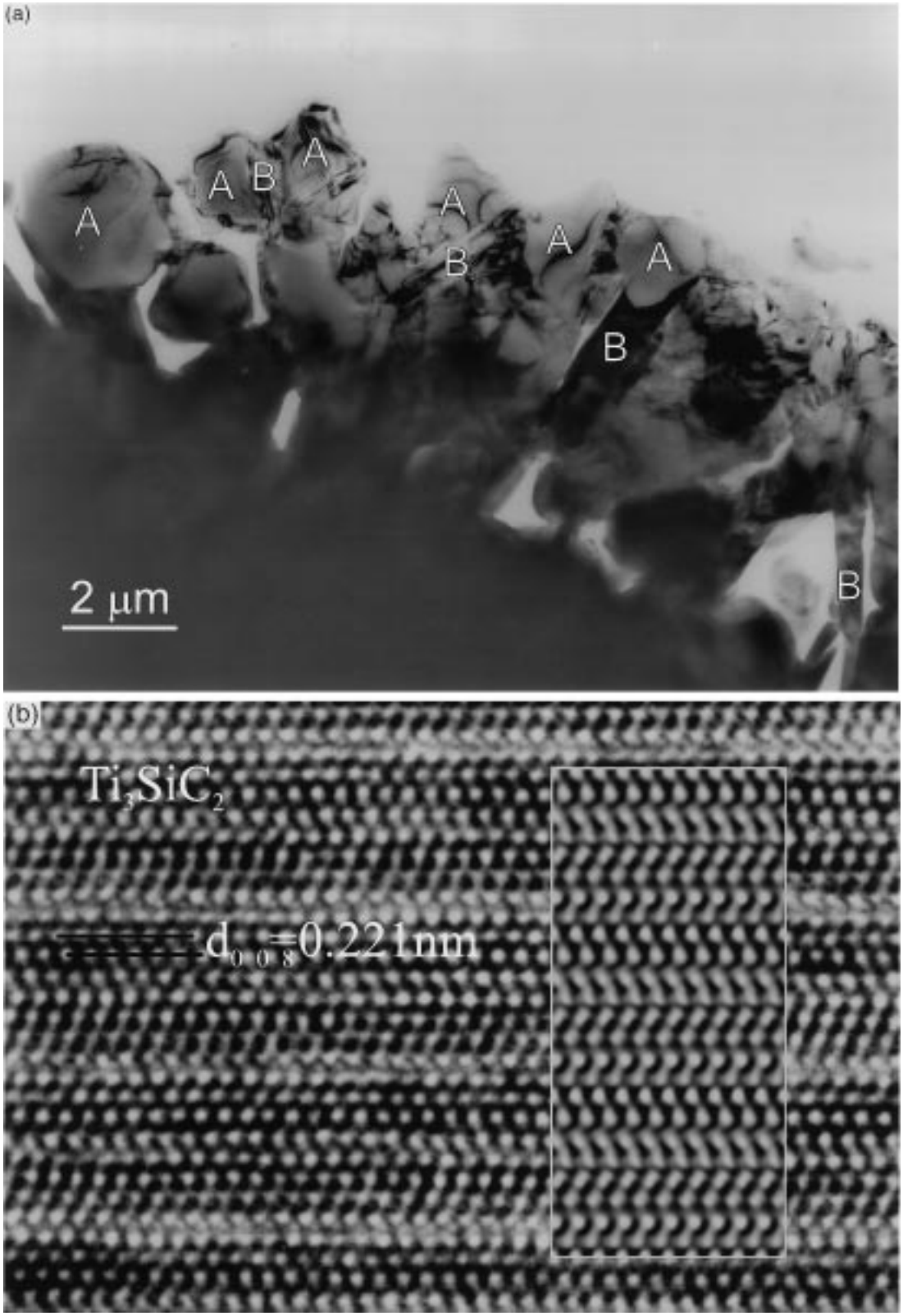


Fig. 3. (a) Bright-field TEM image showing an overview of a cloud-like reaction layer in which mainly spherical TiC grains and $Ti_3SiC_2$ plates are present. Some of the TiC grains and the $Ti_3SiC_2$ plates are indicated by A and B, respectively. (b) Experimental HRTEM image with simulated image as inset of $Ti_3SiC_2$ formed in enclosed regions between the TiC grains of the reaction layer around the SiC particles.

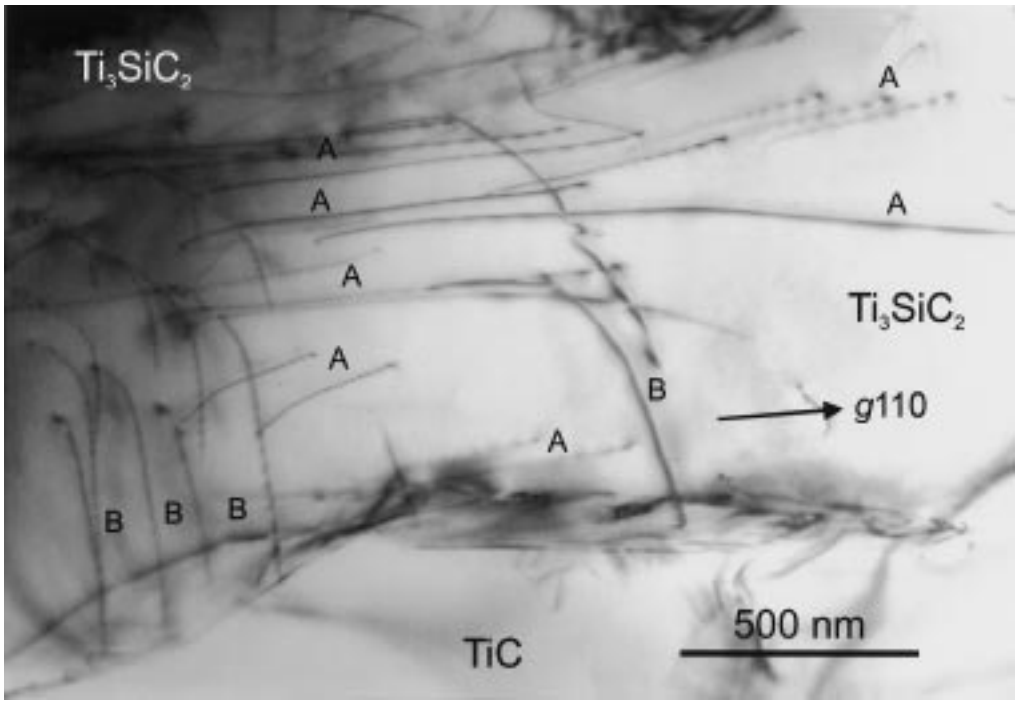


Fig. 4. Two-beam bright-field image (with other strong beam $g11\bar{2}0$ as indicated and with the $Ti_3SiC_2$ crystal tilted about 12° out of the $\langle 01\bar{1}0\rangle$ zone axis) showing dislocations in $Ti_3SiC_2$. The dislocations indicated by A are confined within the basal plane of $Ti_3SiC_2$.

is similar to the mechanism proposed for solid state reactions at the Ti/SiC interface [4, 8] but it is in contrast to Ref. [5]. Also for solid state reactions the phase TiC gives the largest decrease in Gibbs-free energy of the system and is expected to form first. However, for both solidification processes and solid state reactions the actual phases formed of course also depend sensitively on the rate with which different elements are supplied locally and the total amount of different elements available. For instance in the case of a thin Ti film on a SiC surface the reaction products after annealing [6, 7] are different from the case in which the amount of Ti available is more abundant [4, 5, 8].

### *3.3. Precipitation on stacking faults in TiC of the reaction layers*

In a considerable fraction of TiC grains in both types of reaction layers, but predominantly in the cellular layer, a high density of widely extended stacking faults (SFs) of the order of magnitude of 100 nm on TiC {111} planes were observed with TEM; i.e. observations typical for (deformed) material with a very low SF energy. In Figs 5 and 6 two-beam bright-field images are presented of TiC grains with SFs. The SF density in the TiC grains shown in Figs 5 and 6 is still relatively low, but this gives a clearer view than images full with overlapping contrast of SFs also often obtained.

Since the SF energy of TiC is very high and SFs are not observable after severe deformation [23–25], no directly observable SFs were expected in TiC. Depending on the C/Ti ratio the SF energy lies in the range between 130 and 300 $mJ/m^2$ [22]. This would first suggest that the high SF density grains were composed of $\beta$-SiC instead of TiC, because the SF energy of SiC is much lower than that of TiC. This is in accordance with the existence of many SiC poly-types which are based on different stacking sequences of basal hexagonal planes. The crystallography of TiC and $\beta$-SiC is almost identical (both f.c.c. based structures with lattice parameters $a = 0.433$ and 0.444 nm, respectively) and therefore did not allow a precise discrimination between the two phases based on SAED patterns. However, subsequently performed EDS and PEELS analyses in TEM clearly indicated that these originally supposed $\beta$-SiC grains were in fact TiC grains (cf. Fig. 2).

A second possible explanation for the SFs in TiC is the presence of impurities. Planar defects with extrinsic stacking-fault character observed before in TiC were ascribed to the effect of boron impurities [23–26]. Triangular planar defects nucleated at dislocation nodes of networks with $\frac{1}{2}\langle 110\rangle$ Burgers vectors on {111} TiC were identified as very thin $TiB_2$ platelets with hexagonal structure starting possibly as impurity stabilized stacking faults [23–28]. Dissociation of isolated dislocation lines resulting in (widely extended) stacking faults is less frequently observed than the triangular planar faults centred on the dislocation nodes [23, 26–28]. The impurity content of the present TiC grains is locally probably substantially higher than in the

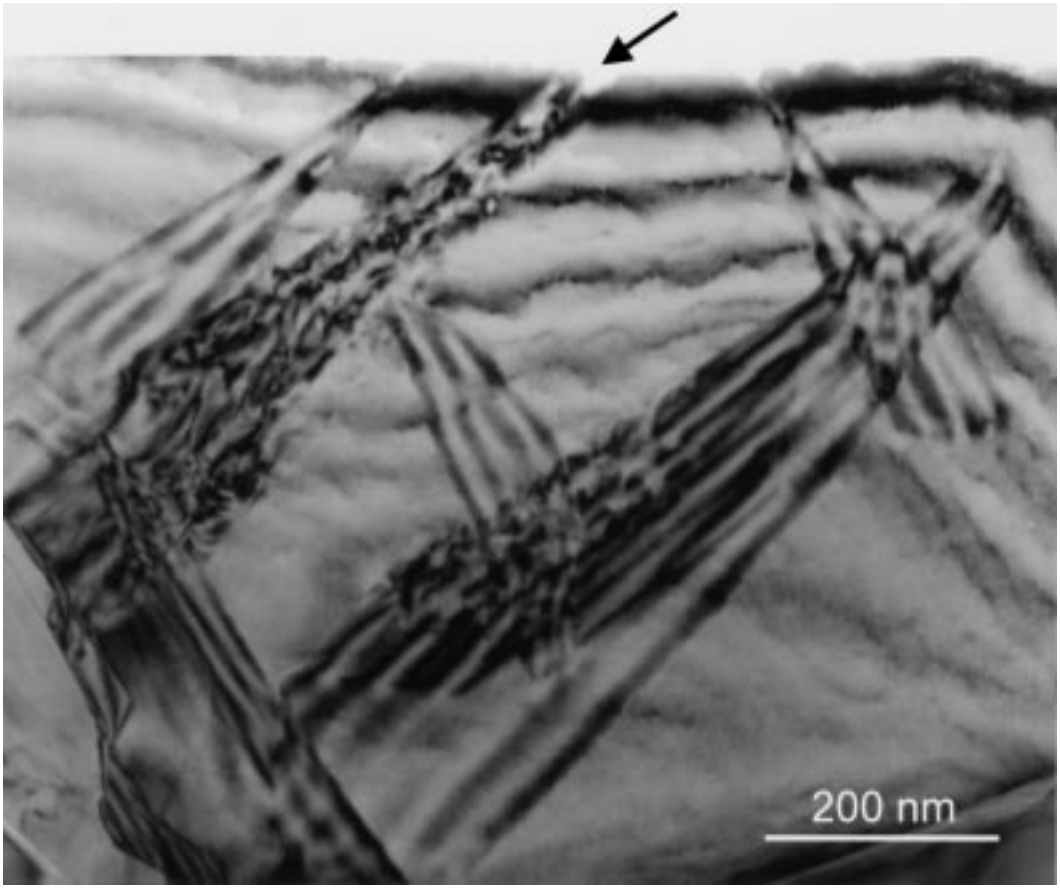


Fig. 5. Two-beam bright-field image showing (unexpected) stacking faults in TiC on {111}. The arrow points at an SF where the usual alternation of bright and dark fringes is distorted by the presence of small precipitates.

above TiC material containing additional traces of boron. Hence a strong reduction of the SF energy is thus well conceivable explaining the observed high density of widely extended SFs. Particularly Si, released during the reaction $SiC + Ti \longrightarrow TiC + Si$, may be enclosed in the TiC grains and may reduce the SF energy. The idea that TiC in reaction layers adjacent to SiC contains a high Si content was earlier proposed in Ref. [8], without any clear evidence though.

The observed faults are generally not of simple single-plane intrinsic or extrinsic stacking-fault type as can be clearly observed in the HRTEM image depicted in Fig. 7. The faults are in general complexes of several closely spaced stacking faults also often involving small twinned regions with thicknesses of typically 2–5 {111} planes. A high impurity content in these faults is probably responsible for their deviation from pure stacking-fault character. Detailed two-beam bright- and dark-field images and (many-beam) HRTEM images revealed the presence of small precipitates on many SFs in the TiC grains with an extension perpendicular to the SF plane usually below 20 nm. The regularly spaced bright and dark fringes associated with "clean" SFs imaged in two-beam BF and DF as often observed, become largely distorted by the presence of these precipitates at the SFs. The arrow in Fig. 5 and the upper white arrow in Fig. 6(a) indicate such SFs where the alternating bright and dark fringes are distorted by the presence of precipitates on the SFs. Also SFs with nearly edge-on orientation with respect to the viewing direction, which in the case of a clean SF correspond to a single hardly observable line, show due to the presence of the precipitates strain-field contrast extending long distances away from the defect plane. A clear example of this phenomenon can be observed in Fig. 6(b) and is indicated by the white arrow. In fact, the visibility of all three about 1 $\mu$m long nearly edge-on SFs in Fig. 6(b) is strongly enhanced by their decoration with precipitates. These long-range strain fields indicate at least partial coherence of the precipitates with the TiC.

Due to the limited size of the precipitates the identification of their phase is difficult. One relatively large lenticular-shaped precipitate (length 250 nm and maximum width of 25 nm) could be identified unambiguously on the basis of an SAED pattern as $Ti_5Si_3$ viewed along the $\langle 11\bar{2}3 \rangle$ direction.

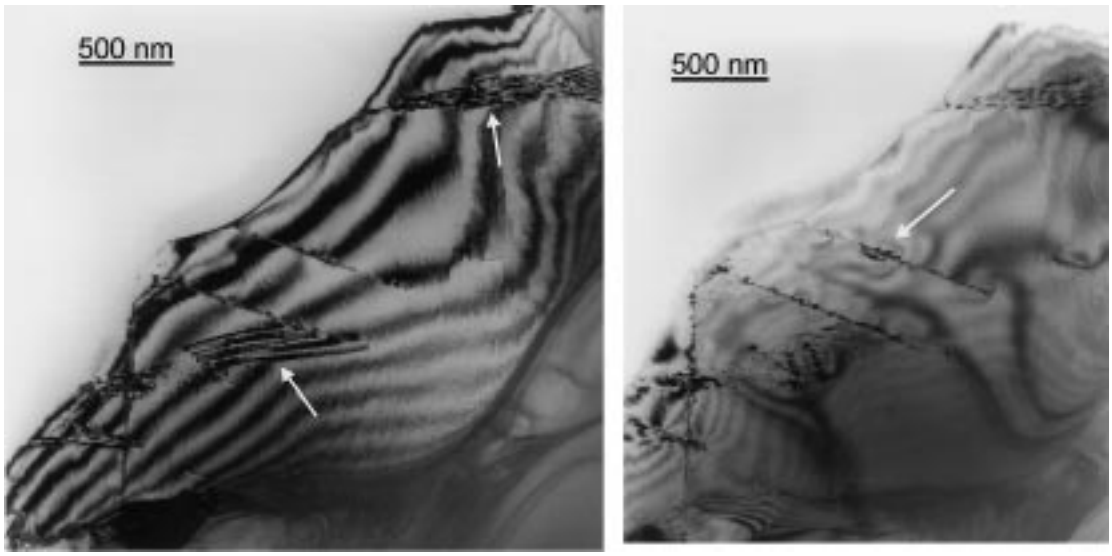


Fig. 6. Two-beam bright-field images showing the same TiC grain of the reaction layer containing (unexpected) stacking faults in TiC on {111}. (a) A two-beam condition with $g200$ near to a ⟨110⟩ zone axis of TiC. The lower white arrow indicates a widely extended SF and the upper white arrow indicates a SF where the usual alternation of bright and dark fringes is distorted by the presence of precipitates nucleated on the SF. (b) A two-beam condition with $g220$ near to a ⟨110⟩ zone axis of TiC. The white arrow indicates a clear example of contrast due to long-range strain fields around precipitates nucleated on a SF. Three long nearly edge-on SFs can be observed and the visibility of these SFs largely originates from their decoration with precipitates.

Three examples of precipitates nucleated on SFs as imaged by HRTEM are depicted in Fig. 8. Using the known interplanar spacings of TiC as reference, the lattice spacings in the precipitates could be determined accurately in the HRTEM images. In Fig. 8(a) the precipitate corresponds to $Ti_5Si_3$ viewed along the $\langle 11\bar{2}3\rangle$ direction and appears to be nucleated on the crossing of two edge-on seen stacking faults in the TiC. The orientation relation (OR) between the precipitate and matrix is such that $\{1\bar{2}12\}Ti_5Si_3//\{200\}TiC$ and $\langle 1\bar{2}1\bar{3}\rangle Ti_5Si_3//\langle 011\rangle TiC$. The mismatch between the $\{1\bar{2}12\}Ti_5Si_3$ and {200}TiC is only about 2.2% and these planes give the impression of continuing (semi-coherently) across the interface. In Fig. 8(b) the precipitate corresponds to $Ti_5Si_3$ viewed along the $\langle 14\bar{5}0\rangle$ direction and the OR and interface orientation are: $(0001)Ti_5Si_3//\{11\bar{1}\}TiC$ and $\{14\bar{5}0\rangle Ti_5Si_3//\langle 011\rangle TiC$. The precipitate has a large aspect ratio with very large (0001) facets parallel to the original stacking fault plane of TiC on which it is nucleated. The spacing between the atomic columns along the interface as seen end on in the HRTEM image is 0.244 nm for $Ti_5Si_3$ and 0.265 nm for TiC also corresponding to a relatively small mismatch. Actually, in Fig. 8(c) two $Ti_5Si_3$ precipitates are merged. One of these precipitates with its interface parallel to the {111}TiC on which the SF occurred, is viewed along its $\langle 11\bar{2}3\rangle$ axis, i.e. the same as for the precipitate in Fig. 8(a). However, this precipitate has the same shape as the one in Fig. 8(b), but now the $\{10\bar{1}0\}$ instead of the (0001) plane of $Ti_5Si_3$ is parallel to the {111} of TiC. The examples of Fig. 8 show that the precipitates can nucleate and grow with a variety of orientations with respect to the TiC matrix and the SF present. The combined SAED and HRTEM information clearly indicate that the precipitates nucleated on SFs in TiC correspond to $Ti_5Si_3$. The precipitates shown in Fig. 8 are already well developed and it should be realized that all the stages in between stacking faults and of these well developed precipitates are actually present in the TiC.

The nucleation of the $Ti_5Si_3$ precipitates on SFs in TiC indicates that the TiC is supersaturated with Si. Apparently, apart from the rejection of the excess Si in the molten matrix, Si also appears to become trapped in the TiC when it is formed at high temperatures (2500–3000°C). At these high temperatures the solubility of Si in TiC is unknown, but at 1200°C the solubility is very small according to the ternary Ti–Si–C phase diagram. So, during cooling the supersaturated Si likes to segregate out of the TiC. A possible mechanism to achieve this within the TiC grains is that Si induces SFs in the TiC and is enriched at these SFs. This mechanism explains the presence of the unusually wide extension and high density of SFs in the TiC grains. SFs in face-centred cubic TiC correspond to locally close-packed hexagonal stacking and all the present relevant phases containing Si ($Ti_5Si_3$, $Ti_3SiC_2$ and all but one of the SiC poly-types) are based on this stacking as well. Thus, Si segregated to SFs is expected to be the most stable state for Si in TiC. If the local enrichment of Si to the SFs is sufficiently strong, new phases containing Si tend to nucleate

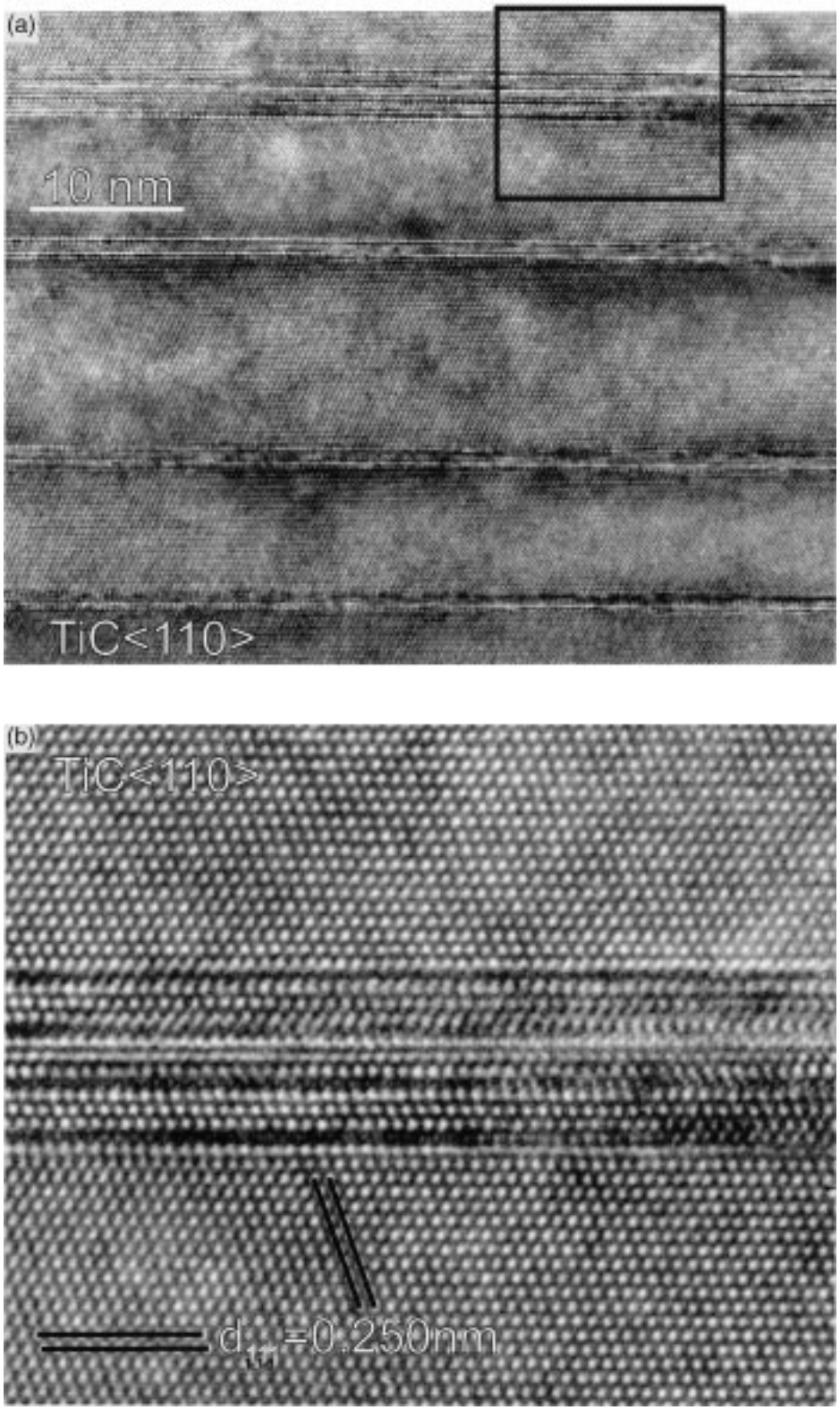


Fig. 7. HRTEM image of TiC in a cellular reaction layer viewed along ⟨110⟩ containing a high density of stacking faults. In the image shown in (a) all SFs are parallel and edge-on observed. In (b) an enlarged part of (a) is shown. The faults are not of simple intrinsic or extrinsic type, but are complexes of closely spaced faults also often containing small twinned regions of two to five {111} planes. Within these faults a strong Si enrichment is probably present.

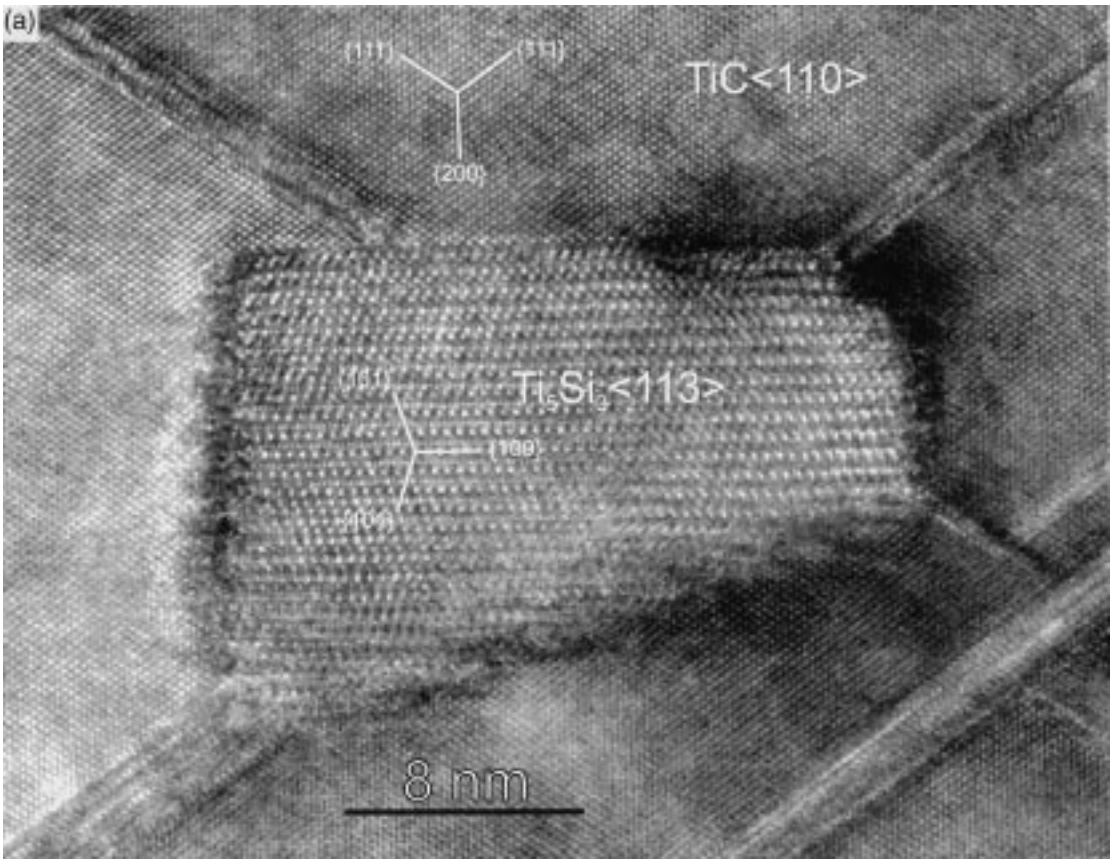


Fig. 8. HRTEM images of $Ti_5Si_3$ precipitates nucleated on stacking faults in TiC present in the reaction layer. The TiC is viewed along the ⟨110⟩ direction. (a) $Ti_5Si_3$ precipitate viewed along $\langle 11\bar{2}3\rangle$ on the crossing of two edge-on observed stacking faults in TiC. (b) $Ti_5Si_3$ precipitate viewed along $\langle 14\bar{5}0\rangle$ having its (0001) plane parallel to the stacking faulted {111}TiC plane. (c) Two merged $Ti_5Si_3$ precipitates. One of these precipitates is viewed along its $\langle 11\bar{2}3\rangle$ axis and the interface is formed by the $\{10\bar{1}0\}Ti_5Si_3$ plane parallel to the stacking faulted {111}TiC plane.

on the SFs during cooling down, explaining the occurrence of the $Ti_5Si_3$ precipitates on the SFs in TiC as observed. According to the ternary phase diagram at 1200°C, excess Si in TiC for Ti/C ratios in between 0.33 and 0.46 will result in the formation of $Ti_5Si_3$. The experimental concentration of C in the TiC of the reaction layers, quantified using EDS and PEELS in the TEM, appeared to be $0.402 \pm 0.022$ and $0.386 \pm 0.011$, respectively, and is in accordance with the observed $Ti_5Si_3$ precipitation on SFs in TiC.

The Si gathered in the precipitates is drained from the SFs in the neighbourhood and subsequently the stability of the remaining SF parts is changed dramatically. These SF parts will have a strong tendency to become unfaulted. Several clear impressions (both in HRTEM and in overviews in BF and DF) were obtained that indeed portions of originally long SFs become unfaulted in the neighbourhood of precipitates. A clear example of an unfaulted part of an SF is already shown in Fig. 8(b) in front of the precipitate's nose, where again at some further distance from the nose the SF and more precipitates become present.

Although the laser treatment does not correspond to thermodynamic-equilibrium conditions, the ternary phase diagram is still useful to predict the reaction products at "interfaces" on a local scale. On the tie-line of SiC–TiC a relatively small increase of the Si content is sufficient to give $Ti_3SiC_2$. Si supersaturating TiC with a carbon content in between 33 and 46 at.% leads to $Ti_5Si_3$ formation. On the tie-line TiC–Ti an increase of the Si content results in $Ti_5Si_3$. Rejection of Si into Ti with small Si concentration gives eutectic $Ti/Ti_5Si_3$ with pre-eutectic Ti and rejection of more than 15 at.% Si results in pre-eutectic $Ti_5Si_3$ instead. All these phase formations taken from the ternary phase diagram, which are in fact the result of the release of Si during the exothermic reaction of SiC with Ti, are in agreement with the observed microstructure after laser embedding of SiC particles in Ti–6Al–4V. Applied with care, similar types of reasoning will hold for, e.g. SiC fibre-reinforced Ti and Ti/SiC diffusion couples.

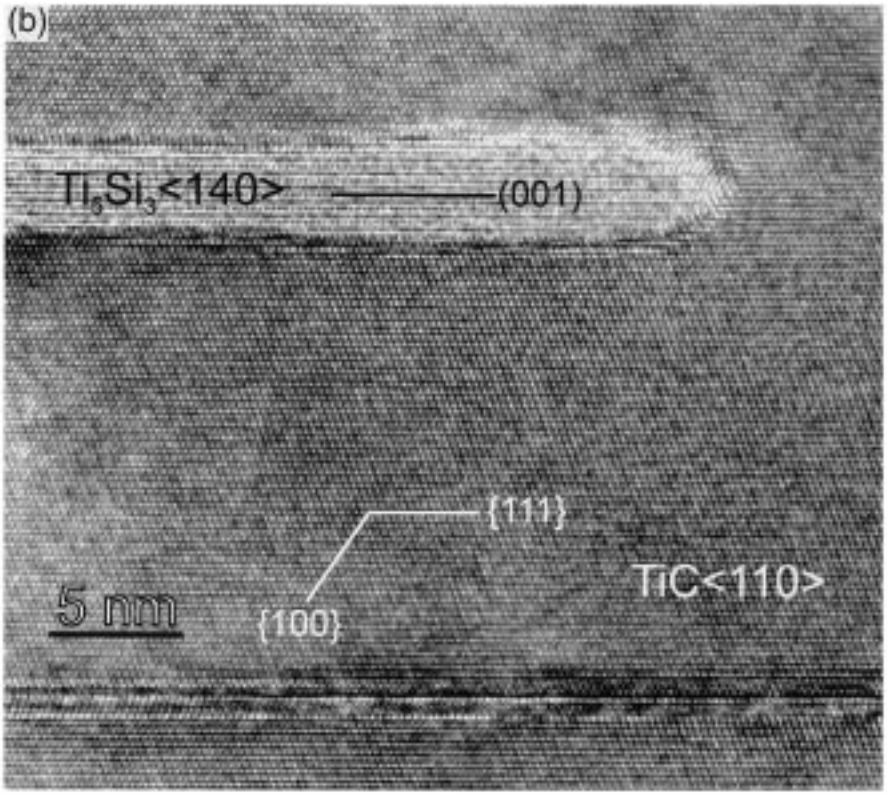


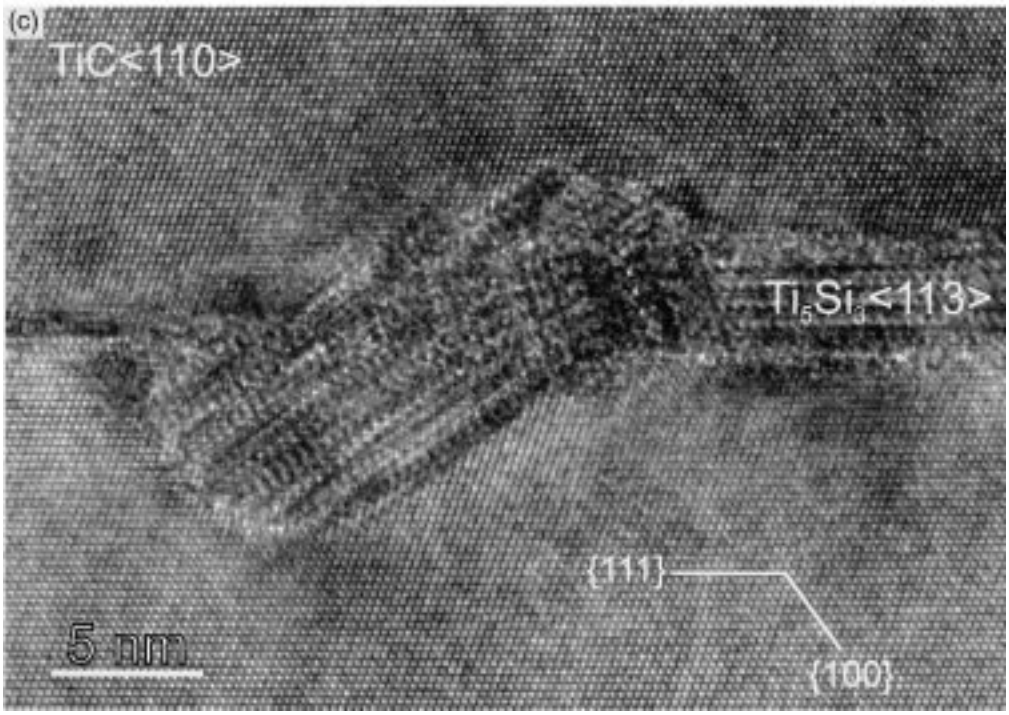


Fig. 8. (*continued*).

## 4. CONCLUSIONS

Laser embedding of SiC particles in Ti–6Al–4V results in reaction layers of TiC around SiC with either a cellular or cloud-like structure. The Si released during the reaction $SiC + Ti \longrightarrow TiC + Si$ is rejected into the melt pool and results in $Ti_5Si_3$ formation. Depending on the extent of local Si rejection pre-eutectic Ti occurs at the bottom and pre-eutectic $Ti_5Si_3$ at the top of the melt pool. If in the cloud-like reaction layer regions in between the TiC grains become enclosed, the rejected Si content increases locally and $Ti_3SiC_2$ plates with dominant (0001) facets nucleate. In the TiC grains particularly of the cellular reaction layer, a high density of widely extending stacking faults is observed and on these faults in many instances small $Ti_5Si_3$ precipitates are present. Firstly the Si supersaturating the TiC induces the SFs and secondly causes the nucleation of $Ti_5Si_3$ precipitates on the SFs. Thirdly, parts of the SFs become unfaulted because the precipitates withdraw Si from the SFs and hence strongly increase the SF energy locally towards the high energy value pertaining to (pure) TiC.

*Acknowledgements*—The National Center for Electron Microscopy of the Lawrence Berkeley Laboratory, U.S.A., in particular Ron Gronski and Uli Dahmen, is gratefully acknowledged for the opportunity to make use of their analytical TEM facilities.

## REFERENCES

1. *Metals Handbook*, Vol. 3, 9th edn. American Society for Metals, Metals Park, OH, 1980, p. 353.
2. Kloosterman, A. B., Kooi, B. J. and De Hosson, J. Th. M., *Acta mater.*, 1998, **46**, 6205.
3. Kloosterman, A. B. and De Hosson, J. Th. M., in *Surface Modification Technologies XI*, ed. T. S. Sudarshan, K. A. Kohr and M. Jeandin. IOM, London, 1997, p. 625.
4. Ratliff, J. L. and Powell, G. W., AFML-TR-70-42 (U.S. Department of Commerce, Springfield, Virginia), 1970, p. 57.
5. Martineau, P., Pailler, R., Lahaye, M. and Naslain, R., *J. Mater. Sci.*, 1984, **19**, 2749.
6. Morozumi, S., Endo, M., Kikuchi, M. and Hamajima, K., *J. Mater. Sci.*, 1985, **20**, 3976.
7. Gottselig, B., Gyarmati, E., Naoumidis, A. and Nickel, H., *J. Europ. Ceram. Soc.*, 1990, **6**, 153.
8. Choi, S. K., Chandrasekaran, M. and Brabers, M. J., *J. Mater. Sci.*, 1990, **25**, 1957.
9. Baker, T. N., Xin, H., Hu, C. and Mridha, S., *Mater. Sci Technol.*, 1994, **10**, 536.
10. Mridha, S. and Baker, T. N., *Mater. Sci Technol.*, 1996, **12**, 595.
11. Abboud, J. H. and West, D. R. F., *Mater. Sci. Technol.*, 1989, **5**, 725.
12. Abboud, J. H. and West, D. R. F., *J. Mater. Sci. Lett.*, 1991, **10**, 1149.
13. JCPDS 29-1128 and 29-1131.
14. Jeitschko, W. and Nowotny, H., *Monatsh. Chem.*, 1967, **98**, 329.
15. Nickl, J. J., Schweitzer, K. K. and Luxenberg, P., *J. less-common Metals*, 1972, **26**, 335.
16. Goto, T. and Hirai, T., *Mater. Res. Bull.*, 1987, **22**, 1195.
17. Arunajatesan, S. and Carim, A. H., *Mater. Lett.*, 1994, **20**, 319.
18. Faber, L., Barsoum, M. W., Zavaliangos, A. and El-Raghy, T., *J. Am. Ceram. Soc.*, 1998, **8**, 1677.
19. Morgiel, J., Lis, J. and Pampuch, R., *Mater. Lett.*, 1996, **27**, 85.
20. Brukl, C. E., Techn. Rep. No. AF ML TR-65-2 part II, Vol. VII. U.S. Department of Commerce, Springfield, VA, 1965, p. 425.
21. Wakelkamp, W. J. J., van Loo, F. J. J. and Metselaar, M., *J. Europ. Ceram. Soc.*, 1991, **8**, 135.
22. Tsurekawa, S. and Yoshinaga, H., *J. Japan. Inst. Metals*, 1994, **58**, 390.
23. Zhao, Q. H., Wu, J., Chadda, A. K., Chen, H. S., Parsons, J. D. and Downham, D., *J. Mater. Res.*, 1994, **9**, 2096.
24. Chien, F. R., Nutt, S. R. and Cummings, D., *Phil. Mag. A*, 1993, **68**, 325.
25. Hollox, G. E. and Smallman, R. E., *J. appl. Phys.*, 1968, **37**, 818.
26. Venables, J., *Physica status solidi*, 1966, **15**, 413.
27. Venables, J., *Phil. Mag*, 1967, **26**, 873.
28. Venables, J., *Metall. Trans.*, 1970, **1**, 2471.